Highlights

- Phase rainbow refractometry (PRR) is developed to measure droplet temperature, size and evaporation rate
- Quantitative relationship between ripple phase shift and size change is theoretical derived
- Transient evaporation rate of n-nonane and n-heptane is experimentally measured and compared with models

Graphical Abstract

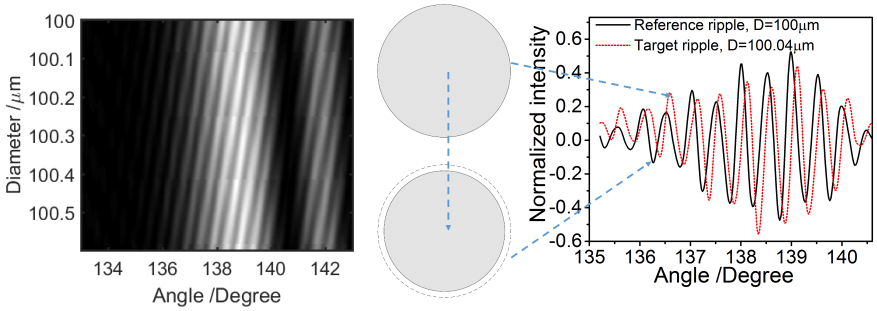

Phase rainbow refractometry image and phase shift of ripple with size changes

Simultaneous measurement of monocomponent droplet temperature/refractive index, size and evaporation rate with phase rainbow refractometry

Yingchun Wu[a,*], Cyril Crua[b], Haipeng Li[c], Sawitree Saengkaew[d], Lutz Mädler[c], Xuecheng Wu[a,*], Gérard Gréhan[d]

[a] *State Key Laboratory of Clean Energy Utilization, Zhejiang University, Hangzhou, 310027, China*
[b] *Advanced Engineering Centre, University of Brighton, Brighton BN2 4GJ, UK*
[c] *Leibniz Institute for MaterialsEngineering IWT,Facultyof ProductionEngineering, University of Bremen, Germany*
[d] *CNRS UMR 6614/CORIA, BP12, 76801 Saint Etienne du Rouvray, France*

Abstract

The accurate measurements of droplet temperature, size and evaporation rate are of great importance to characterize the heat and mass tranfer during evaporation/condensation processes. The nanoscale size change of a micron-sized droplet exactly describes its transient mass transfer, but is difficult to measure because it is smaller than the resolutions of current size measurement techniques. The Phase Rainbow Refractometry (PRR) technique is developed and applied to measure droplet temperature, size and transient size changes and thereafter evaporation rate simultaneously. The measurement principle of PRR is theoretically derived, and it reveals that the phase shift of the time-resolved ripple structures linearly depends on, and can directly yield, nano-scale size changes of droplets. The PRR technique is first verified through the simulation of rainbows of droplets with changing size, and results show that PRR can precisely measure droplet refractive index, absolute size, as well as size change with absolute and relative errors within several nanometers and 0.6%, respectively, and thus PRR permits accurate measurements of transient droplet evaporation rates. The evaporation of flowing single n-nonane droplet and mono-dispersed n-heptane droplet stream are investigated by two PRR systems with a high speed linear CCD and a low speed array CCD, respectively. Their transient evaporation rates are experimentally determined and quantitatively agree well with the theoretical values predicted by classical Maxwell and Stefan-Fuchs models. With the demonstration of evaporation rate measurement of monocomponent droplet in this work, PRR is an ideal tool for measurements of transient droplet evaporation/condensation processes, and can be extended to multicomponent droplets in a wide range of industrially-relevant applications.

Keywords: Phase rainbow refractometry, droplet evaporation rate, temperature, size change, refractive index

*Corresponding author e-mail: wycgsp@zju.edu.cn, wuxch@zju.edu.cn

1. Introduction

Droplets in sprays have tremendous applications in a wide variety of fields, including spray drying in the food industry, pharmaceutical powder production, and the mixing of liquid fuels in automotive and aeronautical combustion systems. In these applications, droplets dynamically evolve in morphology upon breakup from ligaments due to hydrodynamic instability. Besides, droplets can also interact with a surrounding medium through coupled heat and mass transfer processes, such as heating, cooling, condensation and evaporation [1, 2]. In order to gain a comprehensive understanding of droplet dynamics, measurements of transient droplets properties, such as size and temperature, as well as their changes during these dynamic processes, are of essential importance. Hence, a range of optical methods have been proposed based on the complex interactions between light and droplets [3, 4, 5, 6] to measure such properties non-intrusively. With regard to morphology characterization, the non-spherical or even irregular droplets are usually recorded by 2D direct microscopic imaging [7, 8] or 3D digital holographic imaging [9, 10]. In terms of size measurement, in addition to the above two imaging approaches, several interferometric methods have been proposed for spherical droplets. PDA (Phase Doppler Anemometry) is a commercialized instrument for size and velocity measurement for single spherical droplets [11]. Interferometric Particle Imaging (IPI) [12, 13, 14], which was originally proposed as Interferometric Laser Imaging for Droplet Sizing (ILIDS) [15], can measure sizes of droplets in a planar region by analyzing the fringes spacing created by the interference of the droplet's glare points. Morphology-Dependent Resonance (MDR) of a spherical droplet, which is also called Whispering-Gallery Modes (WGM) [16, 17], is a chaotic phenomenon characterized by angularly pulsed peaks with large intensities, and results from constructive interference of multiple light waves that circulate around a sphere's rim via total internal reflections, and return in phase. This only occurs at particular resonant conditions when the optical path length of a round trip inside the droplet is an integral multiple of the exciting light's wavelength. These periodical peaks can be used to measure the droplet size with ultra-high accuracy. As for droplet temperature, it is usually measured with spectroscopic imaging, such as thermal infrared imaging, or Laser-Induced Fluorescence (LIF) which can also be employed to measure species concentration in multicomponent droplets [18, 19, 20].

The evaporation rate of a droplet, as characterized by the well-known D^2-law, is an issue of great importance, and has been intensively documented [1, 21, 22]. Experimental droplet evaporation rates are usually determined by attaching a droplet onto a fiber, and tracking its change of size with time [23, 24, 25]. This is a prevailing approach and can be operated at elevated temperatures and pressures. For this approach, the studied droplets tend to be relatively large with initial sizes up to a millimeter. These droplets are much larger than those typically found in combustion systems, which are in the order of tens of microns or less. The attachment to a fiber affects the evaporation rate through the conduction of heat, but also through the modification of the droplet's external area and shape by surface tension, which in turn affect the

exchange of heat with the surrounding gas. Moreover, the effects of droplet relative velocity with respect to its surrounding, which could be up to dozens and or even hundreds of meters per second in certain engines, cannot be taken into account because the droplet is statically hanged. The suspended method cannot be applied to droplet streams with different spacing parameters [26]. Another approach is to employ sessile droplets to measure the evaporation by monitoring the surface regressions, e.g., via direct imaging or interferometry [27], or even from the vapor gradient by phase measurement using interferometry [28]. Single droplets can also be fixed to study their evaporation by other non-contact methods, such as optical levitation [29, 30, 31]. Some experimental measurements of transient evaporation rate of individual moving fuel droplets [14, 32, 33, 34, 35] and mono-disperse droplet streams [17, 36, 37, 38] have also been reported. The experimental strategy can be classified into two categories. One is a Lagrangian strategy to track the droplet absolute size from multiple samplings. For example, Marié *et al.* [35] measured the fast evaporation process of a falling diethyl ether droplet by combining a high-speed Digital Holographic Particle Tracking Velocimetry (DHPTV) system to track the size and rainbow refractometry to measure the temperature. This strategy is suitable for relatively large size changes, which requires a fast evaporating droplet or long observation times. The other strategy is to directly measure the size change (mass loss) caused by evaporation of a single droplet. Actually, the size change can be regarded as the mass transfer of the evaporating/condensing droplet with its surrounding, and thus is of crucial significance in the characterization of heat and mass transfer of fuel droplet evaporation. MDRs of scattering [17, 30] or fluorescence [17, 29] are usually used for precise identification of evaporation rate via size changes. Recently, PHase Interferometric Particle Imaging (PHIPI) [14] was proposed to measure the absolute diameter, as well as the diameter changes (evaporation rate), of single droplets by analyzing the time-resolved dynamic light scattering in the forward direction.

Rainbow refractometry [38, 39, 40, 41, 42, 43] is a method to simultaneously measure the refractive index and diameter of a droplet by analyzing the light scattering around the rainbow angle. This technique has been applied to determine other droplet parameters on which the refractive index depends, including temperature [44, 45, 46, 47, 48, 49], and species composition and concentration [31, 50, 51, 52]. It was first proposed in the form of the Standard Rainbow Technique (SRT) [39] to measure individual spherical droplets or identical droplet streams only, because the rainbow pattern is highly sensitive to droplet sphericity and small non-sphericity can bring about severe distortions [53, 54, 55]. In order to capture light scattering of a single droplet in a spray and to avoid interference from other droplets, one droplet in the probe volume is isolated using a small pinhole and a short exposure time. Later, the technique was adapted to measure the average refractive index and size distribution of a dense droplet field with dispersed sizes, which was realized by enlarging the pinhole size and extending the exposure time. This particular approach is called Global Rainbow Technique (GRT) [40]. The rainbow signal in GRT integrates rainbows of a large number of droplets, with the individual ripple structures being averaged out. This results in a smooth Airy rainbow that counterbalances the sensitivity to droplet sphericity. Both SRT and GRT are point probe

measurements defined by the pinhole. Recently, One-dimensional rainbow refractometry, which extends the measurement volume to a one-dimensional line section, has been proposed and implemented with two different configurations in both spatial [41] and Fourier domains [42]. One-dimensional rainbow refractometry can be operated in both SRT [38, 42, 56] and GRT modes [41, 42]. Moreover, it is found that the phase of rainbow is extremely sensitive to minute changes in droplet size and refractive index. The phase shift of the ripple structures in rainbows of single droplets or mono-dispersed droplet streams can be recorded with one-dimensional rainbow refractometry as droplets flow along the probed line section, and thus has been applied to simultaneously measure droplet refractive index, size and their changes. The ripple phase shifts with respect to nano-scale changes was also noticed by Sankar *et al.* [36] and Han *et al.* [57]. This approach is named Phase Rainbow Refractometry (PRR) [38], since it uses the phase information of the rainbow signal, in additional to the amplitude and frequency information that are used in traditional SRT and GRT. We briefly introduced PRR with a proof-of-concept validation but without detailed description [38].

Here we present a comprehensive investigation of the development of the PRR technique as well as its application to simultaneously measure droplet temperature via refractive index, diameter, and diameter changes and thereafter evaporation rate of spherical evaporating droplets. We derive the measurement principle of PRR (Section 2.1), and then the data processing algorithm to retrieve the droplet refractive index, size and size changes (Section 2.2). In Section 3 the PRR technique is tested and verified by simulated rainbow images using rigorous Generalized Lorenz-Mie Theories (GLMT). Finally, we present two experimental implementations of PRR for fuel droplets, demonstrating the technique's capabilities for both single droplets and continuous droplet streams (Section 4).

2. Phase rainbow refractometry (PRR)

2.1. Principle and derivation

The primary rainbow of a homogeneous and spherical droplet with a refractive index n respective to its surrounding medium can be exactly described by light scattering theory [58, 59, 60], and expressed as an infinite series which integrates all the scattering processes. Reformulating the scattering coefficients, the Lorenz-Mie light scattering can be decomposed into different processes analogous to the view point of geometric optics and equivalently noted as Debye series with different orders p [61, 62], e.g., reflection ($p = 0$, which is computed together with diffraction ($p = -1$) for numerical convergence), transmission ($p = 1$) and refractions with different sequences of inner reflection ($p = 2, 3, 4, ...$). Generally, the primary rainbow comprises two major scattering processes, i.e., refraction with one internal reflection ($p = 2$) and the external reflection ($p = 0$), as illustrated in Fig. 1. The refracted outgoing wave experiencing one reflection at the inner droplet surface has a cubic phase wavefront. Consequently, its interference produces an Airy rainbow,

which is characterized by a main rainbow peak with markedly enhanced intensity and supernumeraries with decreasing intensities. The first rainbow angle [58], which corresponds to the Descartes ray undergoing the minimum angle of deviation (deflection), is

$$\theta_{\mathrm{rg}} = 4\arccos\left(\frac{1}{n}\sqrt{\frac{4-n^2}{3}}\right) - 2\arcsin\left(\sqrt{\frac{n^2-1}{3}}\right). \tag{1}$$

According to Eq. 1, the rainbow position is determined by the droplet refractive index but not affected by droplet size, therefore permitting refractive index measurement from the rainbow angle in rainbow refractometry. The external reflection ($p = 0$) at droplet surface with a coherent monochromatic laser beam illumination is much weaker than the refracted light ($p = 2$) around the rainbow angle, and its interference with the refraction ($p = 2$) generates the ripple fringes, which have a lower amplitude and higher frequency than the Airy structures and thus are superimposed on the Airy peaks. In some special cases, the scattered light of higher orders could also have a comparable intensity around the primary rainbow angle, and then its interference with the above two light waves should be considered. Omitting light scattered from other orders in Debye series, the primary rainbow is described as

$$\begin{aligned}\mathbf{I}_{\mathrm{rb}}^2 = \left|\mathbf{U}_{\mathrm{Debye}}^{p=0} + \mathbf{U}_{\mathrm{Debye}}^{p=2}\right|^2 = \underbrace{\mathbf{U}_{\mathrm{Debye}}^{p=2}\overline{\mathbf{U}_{\mathrm{Debye}}^{p=2}}}_{\text{Airy rainbow}} \\ + \underbrace{\left(\mathbf{U}_{\mathrm{Debye}}^{p=2}\overline{\mathbf{U}_{\mathrm{Debye}}^{p=0}} + \overline{\mathbf{U}_{\mathrm{Debye}}^{p=2}}\mathbf{U}_{\mathrm{Debye}}^{p=0}\right)}_{\text{ripple structure}} + \underbrace{\mathbf{U}_{\mathrm{Debye}}^{p=0}\overline{\mathbf{U}_{\mathrm{Debye}}^{p=0}}}_{\text{negligible}}.\end{aligned} \tag{2}$$

The first term is the self-interference of the refracted light ($p = 2$), corresponding to the Airy rainbow. The angular position of this term is sensitive to the refractive index, and thus it is used to measure the refractive index in both standard and global rainbow refractometry. The second term is the interference between the refraction and reflection, and contains the ripple structures. The third term is the reflection at the outer surface with negligibly small and relatively flat intensity.

The optical paths of the two main parts of the rainbow light: the refraction ($p = 2$) and external reflection ($p = 0$), are illustrated in Fig. 1. The two planes AF and IM in Fig. 1, which are perpendicular to the incident and outgoing light respectively and both tangent to the droplet surface, are the reference input and output planes, respectively. For the first order of refraction, the light (L_{AB}) incident on the droplet surface with an incident angle (θ_1) has an optical path length

$$L_{\mathrm{AB}} = D\,(1 - \cos\theta_1)/2, \tag{3}$$

where D is the droplet diameter. Then it is refracted into the droplet, travels to droplet inner surface with a reflection at point C, and arrives at the surface point K. The optical path lengths of L_{BC} and L_{CK} are equal as a result of symmetry

$$L_{\mathrm{BC}} = L_{\mathrm{CK}} = nD\cos\theta_2, \tag{4}$$

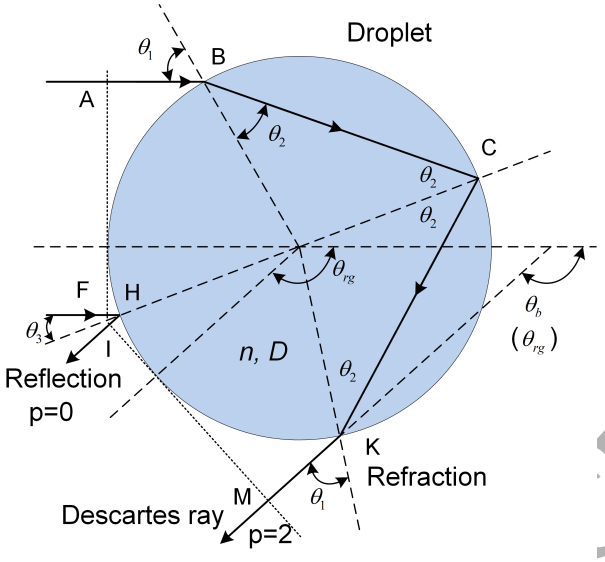

Figure 1: Illustration of optical paths of the refracted light ($p = 2$) and the external reflection ($p = 0$) at rainbow angle $\theta_{\rm rg}$.

where θ_2 is the refracted angle governed by Snell's law

$$n = \frac{\sin\theta_1}{\sin\theta_2}, \tag{5}$$

and the refractive index (n) is multiplied in the optical path length. The light is refracted out of the droplet and propagates to the reference plane IM with an optical path length

$$L_{\rm KM} = D\,(1 - \cos\theta_1)/2. \tag{6}$$

The external reflection incidents on the droplet surface at angle (θ_3), which is parallel to and interferes with the refracted light, has two equal optical path lengths, $L_{\rm FH}$ and $L_{\rm HI}$,

$$L_{\rm FH} = L_{\rm HI} = D\,(1 - \cos\theta_3)/2. \tag{7}$$

Thus, the optical path lengths of refraction and reflection are

$$L_{\rm p2} = L_{\rm AB} + L_{\rm BC} + L_{\rm CK} + L_{\rm KM}, \tag{8}$$

and

$$L_{\rm p0} = L_{\rm FH} + L_{\rm HI}, \tag{9}$$

respectively, and the optical path length difference between them is

$$L_{\rm d} = L_{\rm p2} - L_{\rm p0} = D\,(-\cos\theta_1 + 2n\cos\theta_2 + \cos\theta_3)\,. \tag{10}$$

The subsequent phase difference between the reflection and refraction caused by the optical path length difference is

$$\phi_{\rm d} = \frac{2\pi}{\lambda} L_{\rm d}, \tag{11}$$

where λ is the incident wavelength in the surrounding medium. According to geometric optics, the total deflection angle of the output ray is

$$\theta_{\mathrm{b}} = (p-1)\,\pi + 2\theta_1 - 2p \arcsin\left(\frac{\sin\theta_1}{n}\right), \tag{12}$$

where $p = 2$ for the primary rainbow. And the relationship for the incident angle of reflection is

$$\theta_3 = \frac{\pi}{2} - \frac{\theta_{\mathrm{b}}}{2}. \tag{13}$$

Note that the phase retardant (ϕ_{d}) is a multivariate function dependent on refractive index (n), droplet diameter (D) and the sampling scattering angle (θ_{b}). The phase variation along scattering angle (θ_{b}) leads to the set of alternating bright and dark fringes, known as the ripple structures, and the angular spacing can be obtained with the first Taylor expansion along θ_{b}

$$\Phi_{\mathrm{b}} = 2\pi \Big/ \frac{\partial\phi_{\mathrm{d}}}{\partial\theta_{\mathrm{b}}} = \lambda \Big/ \frac{\partial L_{\mathrm{d}}}{\partial\theta_{\mathrm{b}}} = \frac{2\lambda}{D\left(\sin\theta_1 + \sin\theta_3\right)}. \tag{14}$$

This relationship can also be interpreted as Young's double slit interference [63], with the distance L_{IE} between the two parallel light from the refracted and reflected glare points of $[D\left(\sin\theta_1 + \sin\theta_3\right)/2]$.

Without loss of generality, let us consider Descartes' ray at the rainbow angle ($\theta_{\mathrm{b}} = \theta_{\mathrm{rg}}$), in which the incident angle ($\theta_1 = \theta_{1,\mathrm{rg}}$) is

$$\cos\left(\theta_{1,\mathrm{rg}}\right) = \sqrt{\frac{n^2-1}{3}}. \tag{15}$$

By substituting Eq. 1, 5, 12, 13, and 15 into Eq. 11 and 14, we can get the angular spacing between the fringes at the rainbow angle

$$\Phi_{\mathrm{rg}} = \frac{3^{3/2}\lambda n^2}{D\left(2+n^2\right)\sqrt{4-n^2}}. \tag{16}$$

According to Eq. 16, the angular spacing of the ripples is inversely proportional to the droplet size, and thus can be used for droplet sizing, which resembles the IPI/ILIDS technique. The phase difference between the two light waves can also be obtained

$$\phi_{\mathrm{d,rg}} = \frac{2\pi}{\lambda} D \left(\frac{8+10n^2}{3n^2}\sqrt{\frac{n^2-1}{3}}\right). \tag{17}$$

In Eq. 17, the phase difference is a linear function of droplet diameter. This means that the phase linearly shifts with the droplet size change. Applying a deviation to Eq. 17 and rewriting the droplet size change (ΔD) to the left side, then we obtain

$$\Delta D = c_{\mathrm{rg}} \Delta\phi_{\mathrm{d,rg}}, \tag{18}$$

where the coefficient (c_{rg}) is

$$c_{\mathrm{rg}} = \frac{\lambda}{2\pi} \frac{3^{3/2} n^2}{\left(8+10n^2\right)\sqrt{n^2-1}}. \tag{19}$$

Rainbow refractometry can retrieve the refractive index from the angular position of the Airy rainbow (the first term of Eq. 2), and the droplet size from a combination of the Airy rainbow shape and the ripple structures (the first and second terms of Eq. 2). Here, Eq. 18 reveals that the droplet size change can be measured from the phase shift of the ripple structures (the second terms of Eq. 2). Compared with the traditional rainbow refractometry, this technique extends the capability of droplet size change measurement via phase shift analysis, and is called phase rainbow refractometry (PRR) hereinafter.

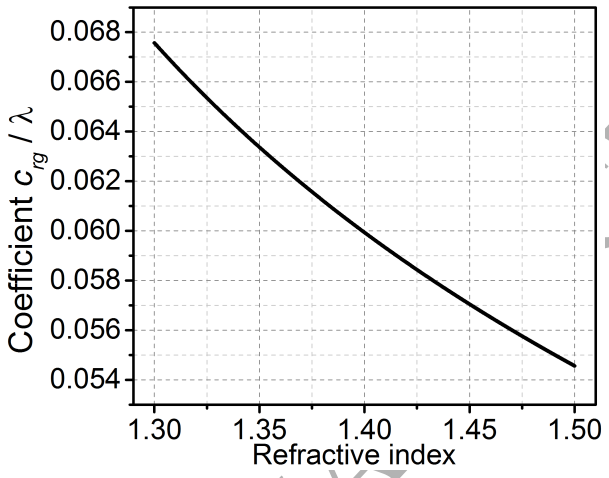

Figure 2: The ratio c_{rg}/λ is monotonically decreasing over the range of refractive indices that are relevant for liquid fuel droplets.

The PRR technique has the following distinguishing merits for the droplet size change measurement.

- Linear response: In the Eq. 18, the size change (ΔD) presents a linear relationship with the phase shift angle ($\Delta\phi_{\mathrm{d,rg}}$). This is remarkable because the formation of rainbow is a highly non-linear process, especially for the Airy rainbow and ripple structures.

- High sensitivity: The coefficient c_{rg} is in the order of one tenth of the wavelength (λ) for common liquids. As shown in Fig. 2, the coefficient decreases with refractive index, with values from about 0.068 at $n = 1.3$ to about 0.054 at $n = 1.5$. Moreover, the resolution of phase shift angles could be easily less than 0.1 radians. Thus, the resolution of the technique can be down to one hundredth of the wavelength, i.e., several nanometres for the visible wavelength. The sensitivity can be also measured by the changes of size parameter, $x = \pi D/\lambda$. The size parameter change Δx can be down to about 0.06 for a size change (ΔD) sensitivity of 10 nm at 532 nm light illumination. The sensitivity of PRR is one order higher than that of MDR, which ranges between 0.6 and 0.8 for common liquids [16].

- Dynamic range: The size change linearly depends on the phase shift, and the accuracy of its retrieval has nothing to do with the droplet size. Therefore the error and uncertainty in size measurement do

not influence the size change measurement. Thus, this technique can be applied to a large range of droplet size spanning from tens to hundreds of microns, as long as the rainbow signal is clearly visible.

2.2. Data processing algorithm

The inversion of the PRR signals involves two parts: to retrieve droplet refractive index and size via an optimal fitting of the standard rainbow signal, and then to measure the phase shift between a pair of ripple structures for the determination of droplet size change. Fig. 3 outlines the flow chart of the PRR inversion algorithm. First, a pair of standard rainbow signals are selected from a PRR image, with one being the reference ($I_{r,rb}$) and the other being the target ($I_{t,rb}$). Both droplet refractive index and size are simultaneously inversed by iteratively searching the optimal fitting of the sampled rainbow signal with the criterion of global minimization

$$\begin{aligned} &\arg\min_{n,D} \left| I_{\mathrm{rb}}(\theta) - I_{\mathrm{c,rb}}(n, D, \theta) \right|, \\ &s.t.\ n \in [n_{\min}, n_{\max}], D \in [D_{\min}, D_{\max}]. \end{aligned} \tag{20}$$

The candidate rainbow $I_{\mathrm{c,rb}}(n, D, \theta)$, is the light scattering around the rainbow angle and can be calculated with different rainbow theories, e.g., Lorenz-Mie scattering theory [59], Debye series [61, 62] or Nussenzveig's complex angular momentum (CAM) theory [64, 65] which is a semi-classical scattering model of rainbows with an accuracy comparable to the Debye series, but with a significantly higher computation efficiency. The Brent's method is adopted for the search optimization, to yield the optimized parameters (n, D) until the residual is less than a preset threshold. The first part is the same as that of the traditional standard rainbow refractometry.

Then, the Airy rainbow (I_{ar}) of the retrieved droplet refractive index and diameter is calculated by taking only the refraction ($p = 2$) into account. Note that the Airy rainbow can be computed with Debye series, CAM theory or Airy theory. Although the rainbow signals calculated with the three theories have small differences, using any of the three does not affect the measurement result. After that, the ripple structures are obtained by subtracting the computed Airy rainbow from the rainbow samples

$$\begin{aligned} I_{\mathrm{r,rp}} &= I_{\mathrm{r,rb}} - I_{\mathrm{ar}}, \\ I_{\mathrm{t,rp}} &= I_{\mathrm{t,rb}} - I_{\mathrm{ar}}, \end{aligned} \tag{21}$$

where $I_{\mathrm{r,rp}}$ and $I_{\mathrm{t,rp}}$ are the reference and target ripple structures, respectively. The phase shift between the two ripples is determined from their cross power spectral density (CPSD) $\Gamma_{\mathrm{rt}}(f)$, which is calculated as follows

$$\Gamma_{\mathrm{rt}}(f)\{I_{\mathrm{r}}, I_{\mathrm{t}}\} = F[\gamma_{\mathrm{rt}}](f) = A_{\mathrm{rt}}(f) \exp[i\phi_{\mathrm{rt}}(f)], \tag{22}$$

where F is the Fourier transform, f is the angular frequency, and $\gamma_{\mathrm{rt}} = \mathrm{E}\left[\left(I_{\mathrm{r}} - \overline{I_{\mathrm{r}}}\right)\left(I_{\mathrm{t}} - \overline{I_{\mathrm{t}}}\right)\right]$ is the cross covariance function, with E the mathematical expectation and the overbar denoting the average. The

amplitude spectrum (A_{rt}) of CPSD has the global largest peak at the coherent frequency (f_{c}). The value of the phase spectrum at their significantly coherent frequency, $\phi_{\mathrm{rt}}(f_c)$, is the phase lag between the two ripples. Hence, the phase shift ($\Delta\phi_{\mathrm{d,rg}}$) can be evaluated

$$\Delta\phi_{\mathrm{d,rg}} = \phi_{\mathrm{rt}}(f_{\mathrm{c}}), \text{ with } \arg\max_{f_{\mathrm{c}}} A_{\mathrm{rt}}(f_{\mathrm{c}}). \tag{23}$$

Substituting the measured phase shift ($\Delta\phi_{\mathrm{d,rg}}$) and refractive index ($n$) into Eq. 18, yields the size change (ΔD). Then the transient droplet evaporation rate can be experimentally determined

$$k_e = \frac{\left[(D+\Delta D)^2 - D^2\right]}{\Delta t} = \frac{2D\Delta D}{\Delta t} + o\left(\frac{\Delta D^2}{\Delta t}\right), \tag{24}$$

where the term $o\left(\Delta D^2/\Delta t\right)$ is negligible and thus omitted.

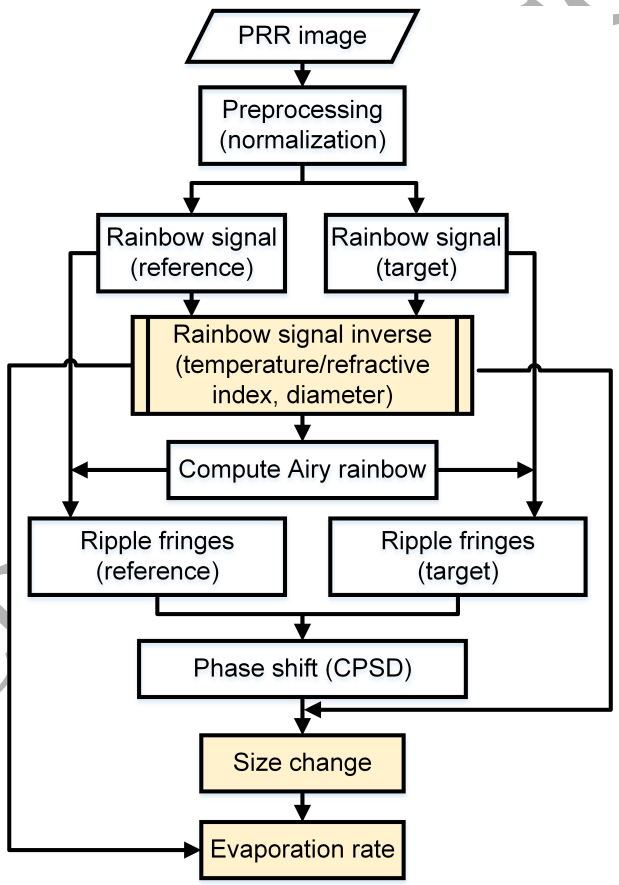

Figure 3: Flow chart of data processing of PRR to measure droplet refractive index, size and size changes simultaneously.

It is worth mentioning that the coherent frequency actually is the frequency of the ripples, and it can be converted to the fringe spacing with the relationship, $\Phi_{\mathrm{rg}} = 2\pi/f_{\mathrm{c}}$. Applying the obtained fringe spacing and refractive index to Eq. 14, the droplet size can also be obtained. This algorithm by counting

fringe frequency/spacing is popular in IPI/ILIDS. It is not necessarily performed because the droplet size is optimally evaluated together with refractive index.

3. Simulation validation

The phase rainbow refractometry is first theoretically tested. Spherical and homogeneous droplets are studied, and the light scattering of droplets under laser sheet illumination is rigorously modeled with Generalized Lorenz-Mie Theories (GLMT) [59], with beam coefficients to model the effects of the laser sheet, which usually is an elliptical Gaussian beam in experiments. The elliptical Gaussian beam is linearly polarized in the y direction, and has a beam waist (ω_x, ω_y) of (1 mm, 25 mm). Previous investigations show that the light scattering can be safely regarded as that under plane wave illumination if the beam waist is much larger than droplet size (usually about five times of the droplet) [59]. In addition, the absolute intensity of droplet light scattering at off-axis positions decreases, as a result of the light power decreasing with the distance from the optical axis in a Gaussian beam, but this effect does not affect the light scattering pattern. In order to ease the data processing, the droplet is placed at the beam waist center in all the simulations to eliminate the effect of intensity drop.

Table 1: List of simulation parameters for the nine different test cases.

case	liquid	n	$D_{\min}$ (μm)	$D_{\max}$ (μm)
1	water	1.333	50	50.6
2	water	1.333	100	100.6
3	water	1.333	150	150.6
4	ethanol	1.360	50	50.6
5	ethanol	1.360	100	100.6
6	ethanol	1.360	150	150.6
7	octane	1.400	50	50.6
8	octane	1.400	100	100.6
9	octane	1.400	150	150.6

The light scattering of the reflection ($p = 0$) and second refraction ($p = 2$) around the primary rainbow angle is calculated in the framework of Debye series. Light scattering of other orders is not taken into account because their influences at this angle are negligible. Table 1 lists the droplet parameters of the nine simulations. In each case, the droplet retains its refractive index, while changes its diameter. Droplets of three liquids, that are, water ($n = 1.333$), ethanol ($n = 1.360$) and octane ($n = 1.400$), are simulated to study the effect of refractive index. For each liquid, three different diameters, i.e., 50 μm, 100 μm and 150

μm, are investigated while droplet diameters change 600 nm with a step of 5 nm. Fig. 4 exemplifies the simulated PRR images of case 2, 3 (water), 6 (ethanol) and 9 (octane). The light intensity is normalized into 8-bit gray images which represent the exact light scattering according to Lorenz-Mie theory, with the exception of the periodical patterns of morphology-dependent resonances (MDR) which were ignored. MDR is a highly nonlinear process at some specific droplet diameters, and its absence facilitates the measurement of PRR.

In the image of Fig. 4(a), the main peak and the first supernumerary bow of the Airy rainbow as well as the superimposed ripple structures are observed. A comparison of Fig. 4(a) with Fig. 4(b) shows that the angular spacing between ripple fringes of 100 μm droplet is larger than that of 150 μm droplet, exemplifying the decrements of the angular span of main Airy peak and ripple fringe spacing with droplet size. Comparing Fig. 4(b) with Fig. 4(c) and 4(d), it is found that the rainbow position shifts, e.g., from about 138° for water to 142° for ethanol. The ripple structures are tilted as the size changes, but the angular spacing between the fringes remains unchanged for each droplet, therefore the ripples are parallel. The degrees of inclination are different, and fringes of water are steeper than those of octane. This is because the coefficient (c_{rg}) decreases with the refractive index, as shown in Fig. 2. Comparing two rainbow signals for octane droplets with sizes of 100 μm and 100.04 μm (Fig. 5(a)) it is apparent that the ripple is significantly shifted as a result of the 40 nm size change, although the positions and amplitudes of the Airy rainbows are almost unchanged. The two simulated rainbow signals are processed with the aforementioned inversion algorithm, yielding solutions for droplet refractive index and diameter of 1.3297 and 99.7 μm, respectively. The optimal fitting (Fig. 5(b)) is in good agreement with the simulated rainbow signal with both the Airy rainbow and the ripple fringes demonstrating the high accuracy of the inversion process. Inversions of the nine test cases show that the uncertainty on the refractive index is in the fourth digit (i.e., ±0.0002), and approximately ±1 μm for the droplet diameter.

According to Eq. 21, ripple structures are obtained by subtracting Airy rainbows from rainbow signals. Fig. 5(c) compares a pair of ripple structures obtained from the two rainbow signals in Fig. 5(a). Ripples in a pair appear almost the same in amplitude and frequency for both droplets, and exhibit an obvious phase shift. The CPSD of the ripple pair in Fig. 5(c) is shown in Fig. 5(d), with the coherent and phase spectra plotted in the lower and upper parts, respectively. The phase spectrum is quite stable near the global maximum of coherent spectrum with a slow varying rate, making phase shift measurement robust and accurate. The phase shift angle of each ripple signal with respect to the reference ripple signal, i.e., the first row of PRR image, is evaluated, and the profile is shown in Fig. 5(e). The phase shift angle measured with CPSD method spans the interval [- π, π], and this causes the common 2π ambiguity. The raw phase shift angle is corrected by using phase unwrapping, that is, adding $\pm 2\pi$ at the jumps, yielding a smooth profile as shown in Fig. 5(e). It is found that the phase shift angles of droplets of the same refractive index almost overlap for all sizes. This is because the phase shift only depends on the relative size change ΔD but

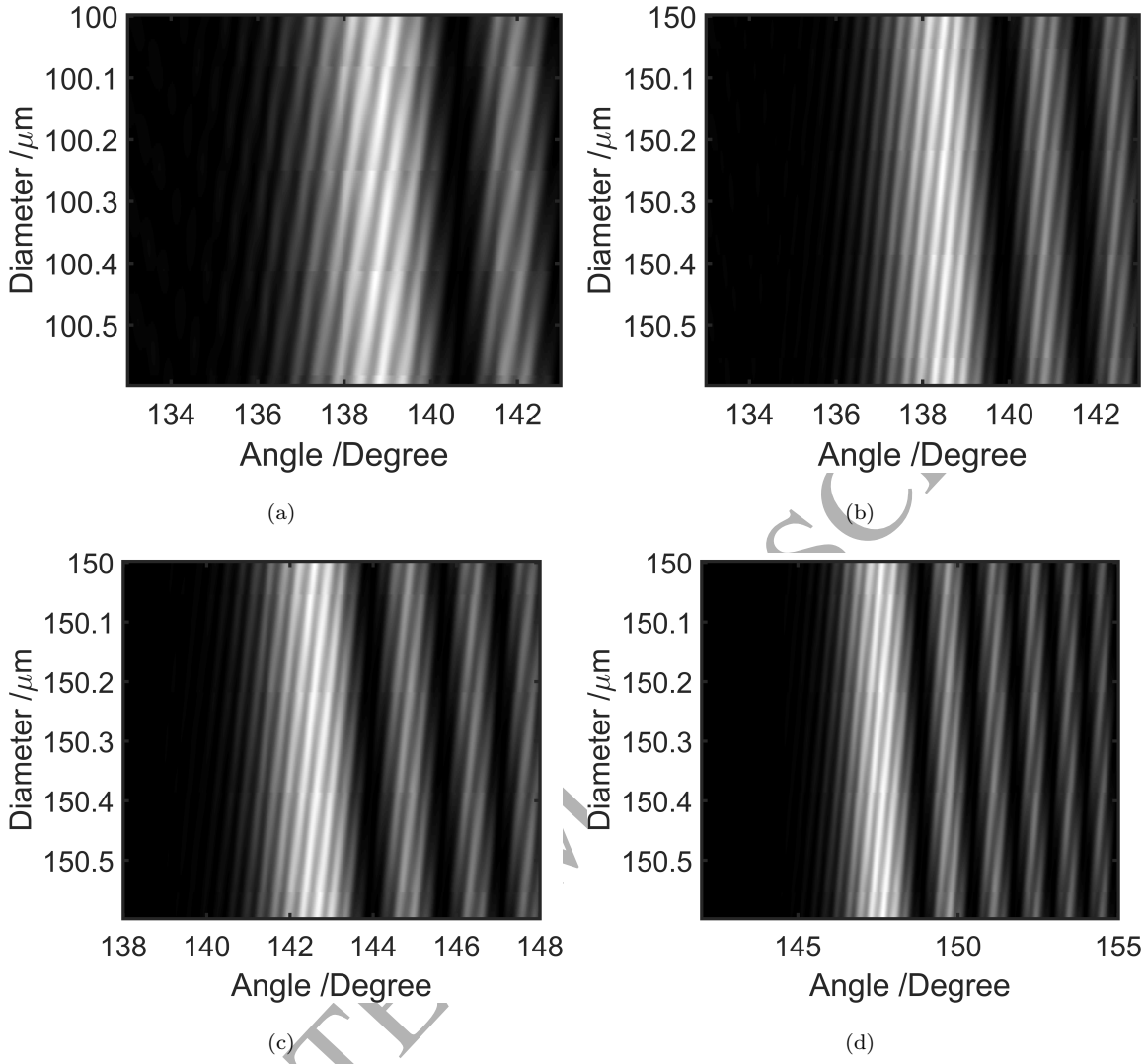

Figure 4: Simulated typical images of phase rainbow refractometry with the laser wavelength of 532 nm, with parameters listed in Table 1. (a) Case 2. (b) Case 3. (c) Case 6. (d) Case 9.

is independent from the absolute size D. It is worth noting that the phase shift angle measured by CPSD is the phase retardant between a ripple pair, but not the absolute phase shift angle in the light scattering direction. With the unwrapped phase shift angles, then the size changes with respect to the size of the first row are determined. The evaluated size changes agree well with the exact values.

The size change measured in nine cases are compared with the exact values, and errors of size change measurement are shown in Fig. 6. The ΔD errors tend to increase gradually with size changes, with values up to 4 nm at 600 nm size change. The tendency is quite linear, and the slopes of linear fitting range between 0.003 and 0.006, and the corresponding relative error is within 0.6%, demonstrating the high accuracy of size change measurements with PRR. Note that the scatterers of ΔD errors closely cluster to each other

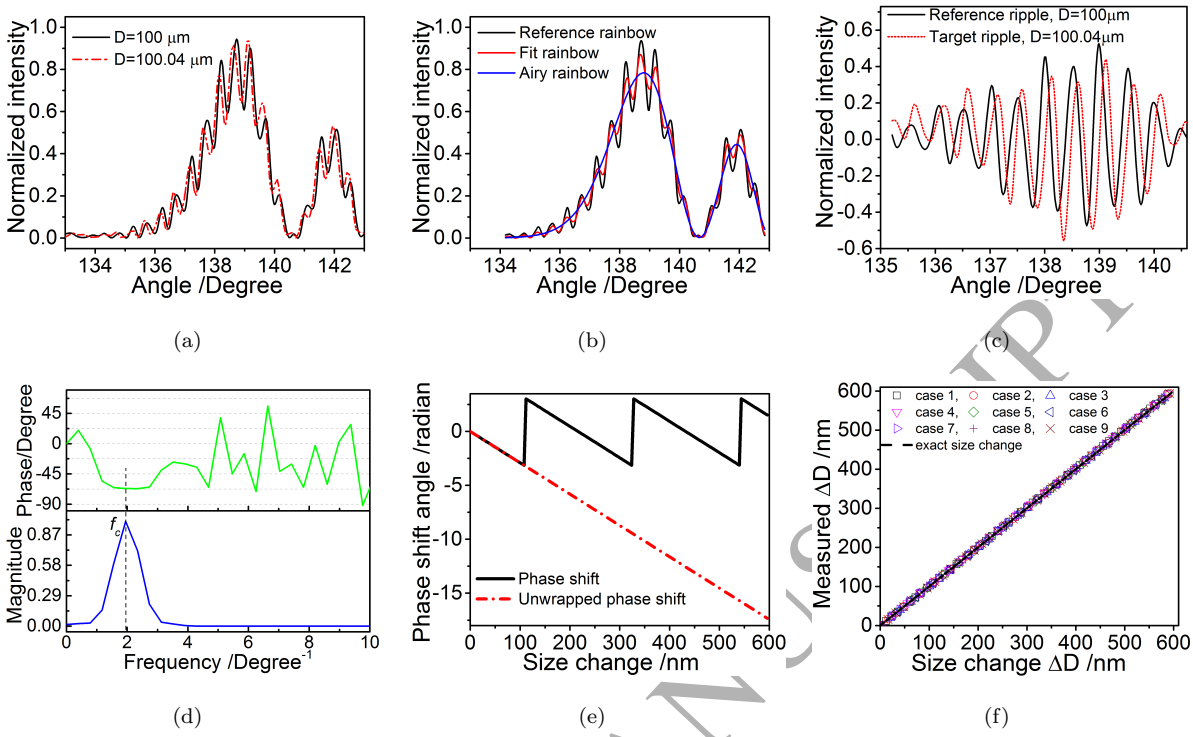

Figure 5: Processing and results of simulated rainbow signals in phase rainbow refractometry. (a) A comparison of a reference (D=100 μm) and a target (D=100.04 μm) rainbow signals of case 2. (b) Optimal fitting of the reference rainbow signal in (a), with n and D of 1.3297 and 99.7 μm, respectively. (c) A comparison of a pair of ripple structures obtained from (a). (d) The amplitude (lower part) and phase (upper part) spectra of CPSD of the ripple pair in (c). (e) The wrapped and unwrapped phase shift angles retrieved from case 2 with CPSD. (f) The size changes measurements of all nine cases in table 1 and their comparisons with the exact values.

and the same accuracy is achieved for the three types of liquids and sizes. This confirms the prediction that the accuracy is not affected by the absolute droplet size. It is also observed that the ΔD errors can exhibit periodic fluctuations which are superimposed on the linear increase with an amplitude of ±2 nm. Besides the limited accuracy of data processing, these fluctuations may result from the discrepancy between the phase shift model based on the simplified geometrical optics and the much more complex real light scattering process of rainbows.

4. Experiments

The PRR technique is implemented with two configurations, and applied to characterize an evaporating single droplet and a droplet stream.

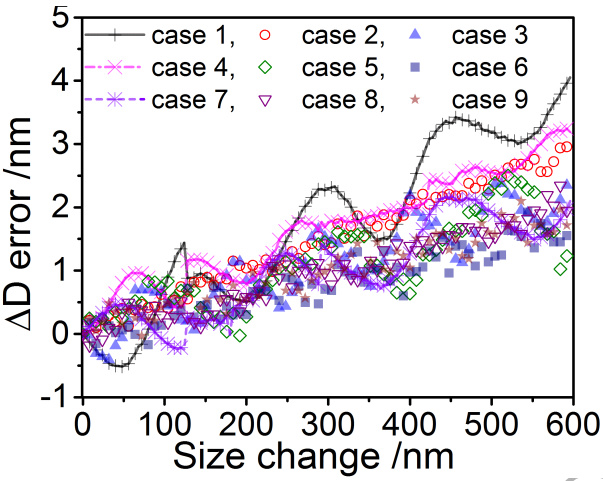

Figure 6: Errors of size change measurements in the nine simulations, with accuracy up to 0.6%.

4.1. Single droplet

Fig. 7 shows the schematics of experimental setup for size change measurements of single droplet with PRR. A droplet-on-demand generator [66, 67] produces identical micron-sized droplets at a frequency of 4 Hz. The droplets were imaged with a microscope to monitor their sizes. Droplets were ejected upward from the generator nozzle in order to prevent nozzle blocking and potential air locks in the nozzle. The droplets had an initial velocity ranging from 0.5 to 1.0 m/s. The generated droplet was illuminated with a continuous wave laser sheet with a wavelength (λ) of 532 nm, and the light scattering by the droplet around the primary rainbow angle was collected by a 1.5 inch spherical lens. A high-speed linear CCD (Spyder3 CL, S3-24-01K40-00-R) was placed on the focal plane of the lens, i.e., 6.56 mm behind the lens. The linear CCD has 1024×1 pixels with a pixel size of 14 μm. The imaging system in this configuration is a Fourier imaging system, and has two advantages. First, the scattered light parallel to the x-z plane, i.e., $\varphi = 90°$, can reach the CCD and is recorded as the rainbow signal, while light at other angles, $\varphi \neq 90°$, cannot be captured by the CCD. This eliminates phase shift caused by changes in the azimuth (φ) angle. Second, the scattered light propagating at the same tilt angle with respect to the optical axis is focused onto the same position of the CCD, as illustrated in Fig. 7. This removes the effect of transversal motions. With these two merits, the light scattering at the same angular positions with respect to the moving and evaporating droplet is captured. The time-resolved light scattering by the droplet during its upward motion was recorded at a frequency of 67 kHz, and each 1024 samples were fused into a PRR image with 1024×1024 pixels (8 bits). The refractive index of n-nonane was measured with an Abbe refractometer with a value of 1.4068 for a wavelength of 532 nm and a temperature of 21°C. Experiments were conducted at room temperature and ambient atmosphere at University of Bremen, and more details can be found in Ref. [49].

Fig. 8(a) displays an experimental PRR image of a single n-nonane droplet (please note that another

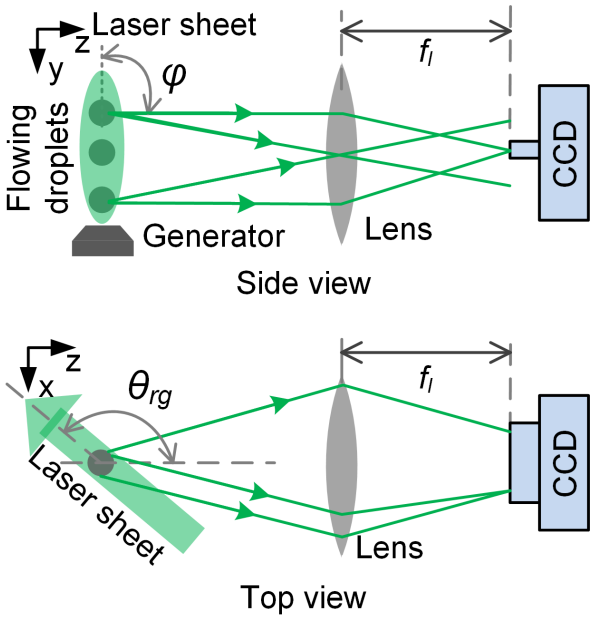

Figure 7: Schematics of experimental configuration of PRR for single droplet measurement [49].

image of the same experiment set was already shown in Fig. 5(a) and Fig. 8 in Ref. [49] for comparison to see the effect of droplet combustion). The amplitude of the rainbow signal first increases to a maximum and then decreases along the height (y) direction. This is caused by the Gaussian distribution of the laser sheet intensity. Fig. 8(b) shows the laser intensity profile obtained by averaging the light scattering of each row of the PRR image. Its Gaussian distribution fitting is plotted as well. The non-uniform effect of the incident laser sheet is compensated by dividing the fitted Gaussian laser sheet, resulting in the normalized rainbow image shown in 8(c). Ripple fringes in both the main peak and first supernumerary bow are clearly recorded. It is observed that there are horizontal fringes in the PRR image, and they are mainly caused by MDRs and non-uniform laser beam. The ripple fringes are slightly tilted, indicating a phase shift and a small size change. A pair of rainbow signals are shown in Fig. 8(d), and processed using the algorithm described above. Fig. 8(e) illustrates a fitting of rainbow signal to inverse the refractive index and size. The retrieved refractive index and diameter has a mean value of 1.4066±0.0003 and 136.7±0.2 μm, respectively, as plotted in Fig. 8(f), and correspondingly the mean droplet temperature is 20.75 °C. The error values in refractive index measurement (average 0.0002) are consistent with the ones in simulations. While the measurement errors in droplet size are smaller than those in simulations, and this can be explained by the fact that prior knowledge on droplet size obtained from microscope imaging is used in inversion. Then the ripple fringes are retrieved and plotted in Fig. 8(g). The phase shift angle is determined using the CPSD method, and then is used for the size change measurement, as the results of Fig. 8(a) shown in Fig. 8(h). Results of size change measurements of fifty PRR droplets are shown in Fig. 8(i). The droplet size decreases with

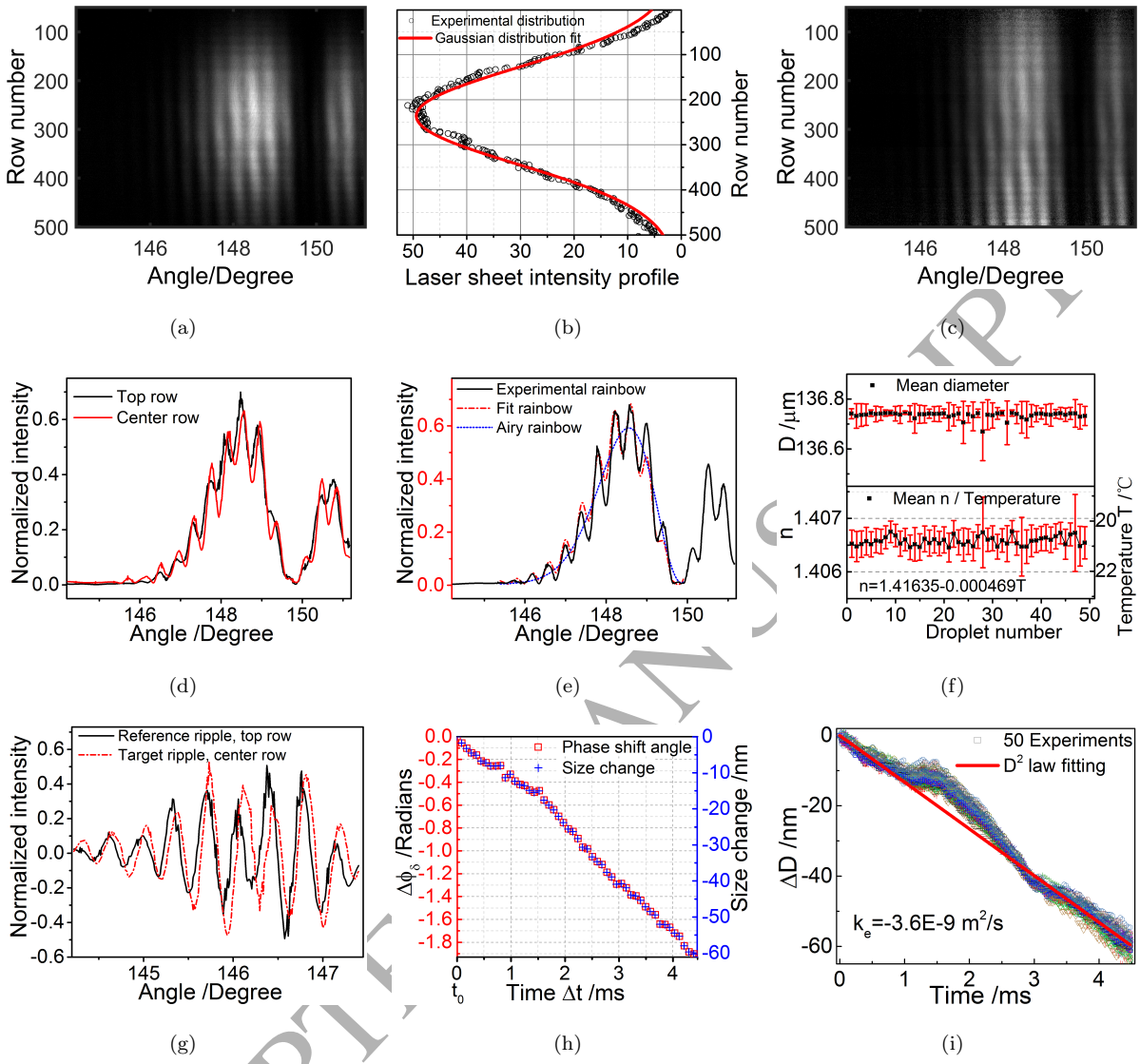

Figure 8: PRR signals of single n-nonane droplets. (a) PRR image of a n-nonane droplet [49]. (b) Intensity profile of the illuminating laser sheet and its Gaussian distribution fitting. (c) Corrected PRR image by compensating laser beam profile, with almost uniform amplitude in rainbow signals. (d) A comparison of two rainbow signals of a single droplet with an interval of 2.24 ms. (e) Inverse process yielding optimized fitting of rainbow signal, with refractive index and size of 1.4066 and 136.7 μm. Airy rainbow of the inversed parameters is also computed. (f) Results of temperature/refractive index and size measurements on fifty sampled droplets. The relationship between n-nonane droplet temperature and refractive index was calibrated in [49]. (g) Illustration of phase shift between the two ripples obtained from (d). (h) Phase shift angles as well as the corresponding size changes obtained from (a). (i) Size changes of the sampled fifty single droplets and the evaporation rate evaluated from D^2-law fitting.

time as a result of evaporation. It is observed that there is a slight discontinuity in the size change at about 1.5 ms for all the studied droplets. Except the effects of other high orders of light scattering and MDR,

this could be partially caused by systematic uncertainty, i.e., non-uniformity of laser sheet, aberrations in imaging system, interferences with droplet light scattering under other illuminations (laser reflections from smooth surfaces), etc. Yet this discontinuity does not hinder the accurate evaluation of droplet evaporation rate. As shown in Fig. 8(i), the D^2-law model is employed to fit the measurements, and the evaporation rate is retrieved with a value of -3.6×10^{-9} m^2/s.

The evaporation rate of the moving n-nonane droplet was theoretically calculated and then compared with the experiments, using the classical Maxwell and Stefan-Fuchs model [1]

$$k_t = 4D_{\mathrm{v}}\frac{\rho_{\mathrm{g}}}{\rho_{\mathrm{l}}}\mathrm{Sh}\,\ln\left(1+B_{\mathrm{M}}\right), \tag{25}$$

where D_{v} is the diffusion coefficient of the n-nonane vapor, and is evaluated by a temperature dependent formula suggested by Fuller's method (Eq. 10 in [68]), with a value of 5.65×10^{-6} m^2/s. The ρ_{g} and ρ_{l} are the densities of gas (a mixture of vapor and air) surrounding the droplet and droplet liquid, respectively. Sh is the Sherwood number and calculated with the correlation suggested by Kalmala et al. [71]

$$\mathrm{Sh} = 2.009 + 0.514\mathrm{Re}^{1/2}\mathrm{Sc}^{1/3}. \tag{26}$$

In Eq. 26, Re is the Reynolds number

$$\mathrm{Re} = \frac{uD}{\nu}, \tag{27}$$

where u is the relative velocity of the gas with respect to the droplet and ν is the kinematic viscosity of the vapor. The Schmidt number Sc is

$$\mathrm{Sc} = \frac{\nu}{D_{\mathrm{v}}}. \tag{28}$$

The Spalding mass transfer number B_{M} is

$$B_{\mathrm{M}} = \frac{(\rho_{\mathrm{vs}} - \rho_{\mathrm{v}\infty})}{\rho_{\mathrm{g}}}, \tag{29}$$

where ρ_{vs} and $\rho_{\mathrm{v}\infty}$ are the mass densities of the saturated vapor at the droplet surface and at an infinite distance from the droplet, respectively, and $\rho_{\mathrm{v}\infty}$ is regarded as zero. All the parameters used for evaporation rate calculation are temperature dependent.

The theoretical evaporation rate of the single moving n-nonane droplet is obtained with a value of k_{t}=-4.1×10^{-9} m^2/s. This is in good agreement with the experimental evaporation rate measured by PRR (k_{e}=-3.6×10^{-9} m^2/s), suggesting that the PRR technique can be a reliable and accurate instrument to measure droplet evaporation rate.

4.2. Droplet stream

In addition to single droplets in the above subsection, droplet streams are also tested with another PRR system. This PRR system was implemented with a one-dimensional rainbow refractometry system, as

schematically shown in Fig. 9. Fig. 9 displays the side and top views of the optical layout. A mono-dispersed droplet stream of n-heptane with size of 100 μm was generated by a droplet generator with an upward speed of about 5 m/s. A laser sheet, whose wavelength was 532 nm, illuminated the droplet stream, and was scattered by droplets. The light scattering was collected by the first lens at a distance of 278 mm with a focal length of 150 mm. The light then passed through a horizontal slit located at the focal plane of the first lens with a width of 1 mm. Similar to the above experiment on single droplet, the first lens and horizontal slit composed a one dimensional filter, and filtered out light scattering without perpendicular incidence in the $y-z$ plane. A second slit, which was vertically orientated, was placed at the image plane of the line section probe volume in order to define the measurement volume. However, this second slit was not strictly essential in our work because the droplet stream was perfectly vertical. The second lens with a focal length of 150 mm conjugated the front surface of the first lens onto the CCD plane, and light scattering of droplets at different heights were directed to and captured by different rows of the CCD sensor (2048×2048 pixels with a pitch of 7.4 μm). One advantage of this configuration is that it permits a direct calibration of the 2D relationship between the pixels of the CCD image and the absolute scattering angles. This calibration is essential to inverse the droplet stream parameters accurately. A more detailed description of the calibration procedures can be found in Ref. [42].

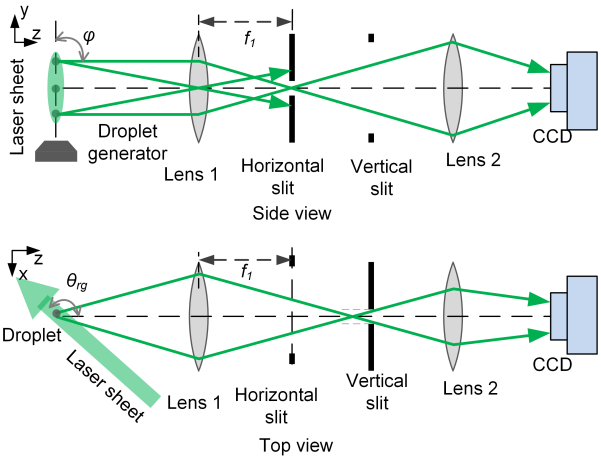

Figure 9: Schematic of one-dimensional phase rainbow imaging system in the $y-z$ and $x-z$ planes [42].

A typical one-dimensional rainbow image of the droplet stream is shown in Fig. 10(a). Two Airy rainbow bows, i.e., the primary peak and the first supernumerary, are recorded and displayed. The ripple structures superimposed inside both peaks are also observed, almost as clearly as for the single droplet image in Fig. 8(a). This demonstrates that the droplets in the stream are almost perfectly identical in both morphology and trajectory. Otherwise the overlapping of rainbow signals of the sampled 1240 droplets would smooth the ripple structures out, leaving only the Airy rainbow aparent, as in the global rainbow technique. Since the

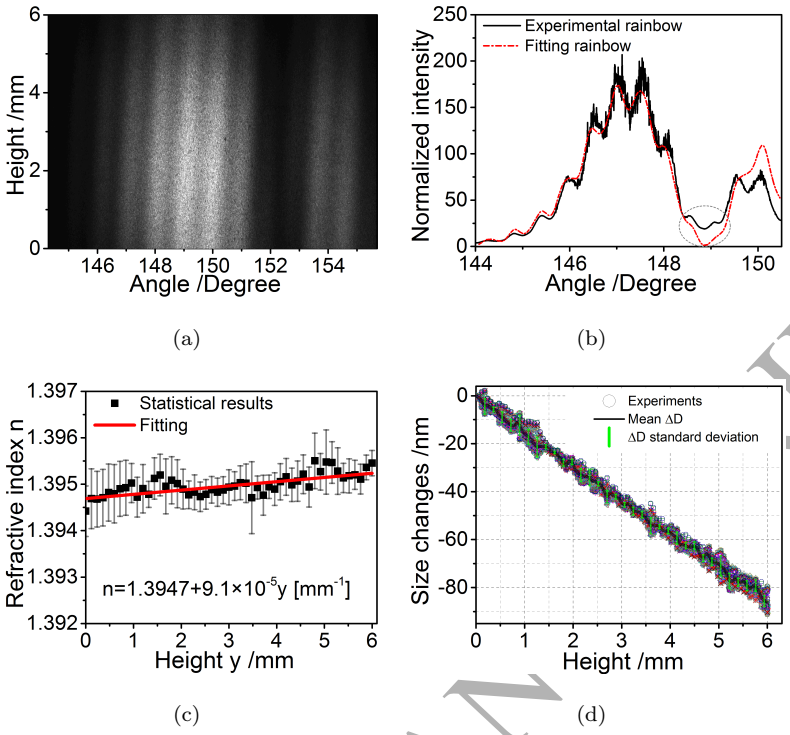

Figure 10: Analysis of the evaporation of a stream of n-heptane droplets by Phase Rainbow Refractometry. (a) One-dimensional PRR image of the droplet stream. (b) Inversion of the rainbow signal to retrieve the refractive index (n=1.3943) and diameter (99.6 µm). (c) Evolution of refractive index with height, with the standard deviations represented by the error bars. (d) Statistical droplet diameter variation of 100 rainbow images, with change rate of 14.3±0.2 nm/mm.

rainbow signals in Fig. 10(a) are almost the same as that in Fig. 8(a), the droplet stream can be assumed as a single droplet in the inverse processing. As shown in Fig. 10(a), the rainbow signal intensities along the vertical axis are affected by the location of the droplet within the laser sheet. Hence the intensity profile of the laser sheet was evaluated to normalize the recorded rainbow image, using the same procedure as the one described in the previous subsection. Individual rainbow signals were extracted from the image using the average of eight consecutive pixel rows, and the averaging window was shifted with a step of four rows to generate the following rainbow. This process resulted in 101 pairs of signals available for processing in each PRR image. Fig. 10(b) shows a typical experimental rainbow signal, and illustrates its inversion to retrieve the optimal droplet refractive index and diameter, with values of 1.3943 and 99.6 µm respectively. The inversed rainbow fits the experimental rainbow well, with the primary and first supernumerary peaks of the Airy rainbow agreeing well in both angular position and intensity profile. The angular positions and frequency of the ripple structures also correspond well.

Despite the excellent overall agreement, we also note some small discrepancies between the experimental and inversed rainbows in Fig. 10(b), as highlighted by the dashed ellipse where the first zero point of

the Airy function and the rainbow should be close to zero. Besides digital noise and aberrations in the imaging system, two factors mainly account for this phenomenon. Firstly, the sampled droplets are not perfectly identical. Minute variations in droplet size cause a phase shift in the ripple structure, and the averaging of the sampled with such phase shifts tends to flatten out the ripple oscillations, reducing the ripple amplitude but also increasing the intensity around the trough position (zero point). Secondly, the interference between the light scattered by neighboring droplets may contribute to non-zero intensities. Since PRR is an out-of-focus imaging system, the light field captured by the camera sensor is an interferometric summary of the light scattering by the droplets in the stream, and the interference among droplets generates fringes as those of Fourier Interferometric Imaging (FII) [69]. In the stream, droplets are equally spaced, and thus the interferometric fringes mainly appear in the vertical direction. The frequencies of these FII fringes are inversely proportional to the droplet spacing. The narrow horizontal slit only allows interference among closely-located droplets. These three mechanisms dramatically reduce the effect of interferometric fringes, which are flattened by the integral of light field over the exposure time and disappear in the PRR image. Another collaborative evidence supporting this argument is the absence of the morphology dependent resonances in the experimental rainbow image. The MDR patterns occur periodically at particular refractive index and diameter. If the sampled droplets are exactly identical, the MDR patterns should be observed at some rows of the recorded rainbow because the droplets vary continuously during their upward movements, however not in Fig. 10(a). This is because the position of the MDR is not stable and then is masked by the rainbow signals of other droplets.

One hundred PRR signals of the n-heptane droplet stream were processed to obtain the evolution of the droplet refractive index and diameter with height (Fig. 10(c)). The refractive indices range between 1.3938 and 1.3956, with a mean value of 1.3950 and a standard derivation of 0.0002, with the accuracy almost the same as those in simulations and single droplet experiments. Despite the uncertainty on the refractive index measurement, the mean value from 100 PRR images exhibits an increasing trend with height, with a gradient of 9.1×10^{-5} per millimeter. This increase in refractive index indicates that the droplet temperature is changing along the upward motion. Since the refractive index of n-heptane is related to temperature with a coefficient of 5.1×10^{-4} K^{-1} at 532 nm [70], the corresponding temperature change can be determined with a value of -0.17 K/mm. The measured droplet diameter is 99.8±1.5 μm, and agrees well with the initial droplet size of 100 μm according to the manufacturer. The deviation is larger than those in simulations and single droplet experiments. Besides the possible tiny variations in initial droplet sizes, it is mainly attributed to the FII feature of the recorded PRR image.

In Fig. 10(a), the ripple structures incline along the height (y) direction, and present an obvious phase shift between the fringes. This is a result of the decrease of droplet diameter caused by evaporation. The phase shift angle and associated size change of the droplet stream are determined with the aforementioned scheme. First the Airy rainbow of the droplet stream is calculated with the above measured droplet refractive

index and diameter, as exemplified in Fig. 5(b). Then the ripple structures are retrieved. The phase shift angle of Fig. 10(a) is evaluated and then used to determine the size change. The phase shift angle increases from top to bottom up by 2.6 radians, corresponding to a diameter decrease of 86 nm. Fig. 10(d) shows that the diameter changes are very similar for all 100 PRR images, with a mean standard deviation of 1.8 nm. This indicates that the droplets within the stream have undergone the same evaporation process. Fitting the D^2-law onto our measurements we obtain a diameter change rate of -14.3±0.2 nm/mm. This enables the calculation of the evaporating rate as -1.43±0.02×10^{-8} m^2/s.

As the monodisperse droplet stream moves upward, the droplets entrain the surrounding air and a flow field is developed. This leads to a significant decrease of the relative velocity between the droplet and the surrounding gas, especially at the upper region of the droplet stream [37]. Meanwhile, a vapor layer surrounding the droplet stream trajectory also develops along the radial direction, with the thickness of the vapor layer increasing with the distance from the nozzle, and with a partial pressure approaching the saturated pressure [72, 73, 26]. Under these two effects, the forced convection induced by the relative speed between the gas and droplet plays a limited and minor role in the radial transfer of vapor. Consequently, the evaporation rate is mainly determined by the diffusion radially away from droplet surface to the ambient gas. This means that the Sherwood number approaches 2 and the Reynolds number approaches zero when applying Eq. 24 for the theoretical evaluation of the evaporation rate. The theoretical evaporation rate is -1.59×10^{-8} m^2/s, and is in good agreement with the experimental value. In this work both the theoretically-derived and experimentally-measured evaporation rates for the droplet stream are much smaller than that of an isolated droplet, and this observation is consistent with previous investigations [26, 74].

5. Conclusions

In this work we demonstrated the measurement principle, numerical validations, data processing algorithm, and experimental implementations of Phase Rainbow Refractometry for the quantification of the evaporation rate of liquid fuel droplets.

We validated the PRR technique by simulating several types of liquids and conditions, to show that it can resolve droplet diameter changes down to several nanometers with an accuracy up to 0.6% for size changes of hundreds of nanometers. These simulations were in agreement with the theoretical predictions.

The technique was then applied onto an evaporating isolated droplet as well as onto a droplet stream. The nano-scale size changes and the transient evaporation rates were determined, and found to be in good agreement with theoretical values.

In addition to measuring the temperature (refractive index) and diameter of homogeneous and spherical droplets, PRR can directly yield their nano-scale size changes by resolving the phase shift of the time-resolved ripple structures. This approach quantifies the size change directly, rather than through the tracking of

absolute droplet diameters with time. The theoretical deviation of PRR reveals that the phase shift in ripple structures linearly depends on the change of droplet diameter but is independent of the absolute droplet size, and thus the measurement accuracy would not be affected by droplet size. The PRR technique can be applied to a large range of applications that rely on droplet evaporation and condensation.

6. Acknowledgments

The authors are grateful to Dr. Thomas Wriedt from IWT (University of Bremen) for fruitful discussions. This work was partially supported by the German Research Foundation (DFG) within Priority Programme SPP 1934 (DiSPBiotech) [Project MA 3333/12-1], and by the UK's Engineering and Physical Science Research Council [grants EP/K020528/1 and EP/M009424/1].

7. References

References

[1] Sazhin S. Droplets and sprays: Springer; 2014.

[2] Sazhin SS. Modelling of fuel droplet heating and evaporation: Recent results and unsolved problems. Fuel. 2017;196:69-101.

[3] Tropea C. Optical Particle Characterization in Flows. Annual Review of Fluid Mechanics. 2011;43:399-426.

[4] Lemoine F, Castanet G. Temperature and chemical composition of droplets by optical measurement techniques: a state-of-the-art review. Experiments in fluids. 2013;54:1-34.

[5] Fansler TD, Parrish SE. Spray measurement technology: a review. Measurement Science and Technology. 2015;26:012002.

[6] Gouesbet G, Gréhan G. Laser-based optical measurement techniques of discrete particles: A review [invited keynote]. International Journal of Multiphase Flow. 2015;72:288-97.

[7] Crua C, Heikal MR, Gold MR. Microscopic imaging of the initial stage of diesel spray formation. Fuel. 2015;157:140-50.

[8] Crua C, Manin J, Pickett LM. On the transcritical mixing of fuels at diesel engine conditions. Fuel. 2017;208:535-48.

[9] Memmolo P, Miccio L, Paturzo M, Caprio GD, Coppola G, Netti PA, et al. Recent advances in holographic 3D particle tracking. Adv Opt Photon. 2015;7:713-55.

[10] Wu Y, Wu X, Yao L, Brunel M, Coëtmellec S, Lebrun D, et al. 3D boundary line measurement of irregular particle with digital holography. Powder Technology. 2016;295:96-103.

[11] Albrecht H-E, Damaschke N, Borys M, Tropea C. Laser Doppler and Phase Doppler Measurement Techniques: Springer Science & Business Media; 2013.

[12] Dehaeck S, van Beeck JPAJ. Designing a maximum precision interferometric particle imaging set-up. Experiments in Fluids. 2007;42:767-81.

[13] Shen H, Coetmellec S, Brunel M. Cylindrical interferometric out-of-focus imaging for the analysis of droplets in a volume. Optics letters. 2012;37:3945-7.

[14] Wu Y, Li H, Brunel M, Chen J, Gréhan G, Mädler L. Phase interferometric particle imaging for simultaneous measurements of evaporating micron-sized droplet and nanoscale size changes. Applied Physics Letters. 2017;111:041905.

[15] König G, Anders K, Frohn A. A new light-scattering technique to measure the diameter of periodically generated moving droplets. Journal of aerosol science. 1986;17:157-67.

[16] Chýlek P. Resonance structure of Mie scattering: distance between resonances. Journal of the Optical Society of America A. 1990;7:1609-13.

[17] Chen G, Mazumder MM, Chang RK, Swindal JC, Acker WP. Laser diagnostics for droplet characterization: Application of morphology dependent resonances. Progress in Energy and Combustion Science. 1996;22:163-88.

[18] Maqua C, Castanet G, Lemoine F. Bicomponent droplets evaporation: Temperature measurements and modelling. Fuel. 2008;87:2932-42.

[19] Maqua C, Castanet G, Grisch F, Lemoine F, Kristyadi T, Sazhin SS. Monodisperse droplet heating and evaporation: Experimental study and modelling. International Journal of Heat and Mass Transfer. 2008;51:3932-45.

[20] Perrin L, Castanet G, Lemoine F. Characterization of the evaporation of interacting droplets using combined optical techniques. Experiments in Fluids. 2015;56:29.

[21] Chen LF, Liu ZX, Lin YZ, Zhang C. Different spray droplet evaporation models for non-ideal multi-component fuels with experimental validation. International Journal of Heat and Mass Transfer. 2016;94:292-300.

[22] Borodulin VY, Letushko VN, Nizovtsev MI, Sterlyagov AN. Determination of parameters of heat and mass transfer in evaporating drops. International Journal of Heat and Mass Transfer. 2017;109:609-18.

[23] Javed I, Baek SW, Waheed K. Evaporation characteristics of heptane droplets with the addition of aluminum nanoparticles at elevated temperatures. Combustion and Flame. 2013;160:170-83.

[24] Ma XK, Zhang FJ, Han K, Yang B, Song GQ. Evaporation characteristics of acetone-butanol-ethanol and diesel blends droplets at high ambient temperatures. Fuel. 2015;160:43-9.

[25] Han K, Zhao CL, Fu G, Zhang FJ, Pang SP, Li YC. Evaporation characteristics of dual component droplet of benzyl azides-hexadecane mixtures at elevated temperatures. Fuel. 2015;157:270-8.

[26] Castanet G, Perrin L, Caballina O, Lemoine F. Evaporation of closely-spaced interacting droplets arranged in a single row. International Journal of Heat and Mass Transfer. 2016;93:788-802.

[27] Verma G, Singh KP. Time-resolved interference unveils nanoscale surface dynamics in evaporating sessile droplet. Applied Physics Letters. 2014;104.

[28] Dehaeck S, Rednikov A, Colinet P. Vapor-Based Interferometric Measurement of Local Evaporation Rate and Interfacial Temperature of Evaporating Droplets. Langmuir. 2014;30:2002-8.

[29] Pastel R, Struthers A. Measuring evaporation rates of laser-trapped droplets by use of fluorescent morphology-dependent resonances. Applied Optics. 2001;40:2510-4.

[30] Roth N, Wilms J, Weigand B. Technique for measurements of the evaporation rate of single, freely falling, droplets. Proceedings of the 12th International Symposium on Application of Laser Techniques to Fluid Mechanics, Lisbon, Portugal2004. p. 1-10.

[31] Wilms J, Weigand B. Composition measurements of binary mixture droplets by rainbow refractometry. Applied Optics. 2007;46:2109-18.

[32] Van Beeck JPAJ, Riethmuller M. Nonintrusive measurements of temperature and size of single falling raindrops. Applied optics. 1995;34:1633-9.

[33] Massoli P. Rainbow refractometry applied to radially inhomogeneous spheres: the critical case of evaporating droplets. Applied Optics. 1998;37:3227-35.

[34] Shanthanu S, Raghuram S, Raghavan V. Transient evaporation of moving water droplets in steam-hydrogen-air environment. International Journal of Heat and Mass Transfer. 2013;64:536-46.

[35] Marié J, Grosjean N, Méès L, Seifi M, Fournier C, Barbier B, et al. Lagrangian measurements of the fast evaporation of falling diethyl ether droplets using in-line digital holography and a high-speed camera. Experiments in Fluids. 2014;55:1-13.

[36] Sankar S, Buermann D, Bachalo W. Application of Rainbow Thermometry to the Study of Fuel Droplet Heat-up and Evaporation Characteristics. Journal of engineering for gas turbines and power. 1997;119:573.

[37] Fieberg C, Reichelt L, Martin D, Renz U, Kneer R. Experimental and numerical investigation of droplet evaporation under diesel engine conditions. International Journal of Heat and Mass Transfer. 2009;52:3738-46.

[38] Wu Y, Promvongsa J, Saengkaew S, Wu X, Chen J, Gréhan G. Phase rainbow refractometry for accurate droplet variation characterization. Optics Letters. 2016;41:4672-5.

[39] Roth N, Anders K, Frohn A. Refractive-index measurements for the correction of particle sizing methods. Appl Opt. 1991;30:4960-5.

[40] Van Beeck JPAJ, Giannoulis D, Zimmer L, Riethmuller M. Global rainbow thermometry for droplet-temperature measurement. Optics letters. 1999;24:1696-8.

[41] Wu X, Jiang H, Wu Y, Song J, Gréhan G, Saengkaew S, et al. One-dimensional Rainbow Thermometry (ORT) system by using slit apertures, Opt. Lett. 2014;39:638-641.

[42] Wu Y, Promvongsa J, Wu X, Cen K, Gréhan G, Saengkaew S. One-dimensional rainbow technique using Fourier domain filtering. Optics Express. 2015;23:30545-56.

[43] Yu H, Sun H, Shen J, Tropea C. Measurements of refractive index and size of a spherical drop from Gaussian beam scattering in the primary rainbow region. Journal of Quantitative Spectroscopy and Radiative Transfer. 2018;207:83-8.

[44] van Beeck JPAJ, Zimmer L, Riethmuller ML. Global rainbow thermometry for mean temperature and size measurement of spray droplets. Particle & Particle Systems Characterization. 2001;18:196-204.

[45] Hom J, Chigier N. Rainbow refractometry: simultaneous measurement of temperature, refractive index, and size of droplets. Applied Optics. 2002;41:1899-907.

[46] Lemaitre P, Porcheron E, Gréhan G, Bouilloux L. Development of a global rainbow refractometry technique to measure the temperature of spray droplets in a large containment vessel. Measurement Science and Technology. 2006;17:1299.

[47] Letty C, Renou B, Reveillon J, Saengkaew S, Gréhan G. Experimental study of droplet temperature in a two-phase heptane/air V-flame. Combustion and Flame. 2013;160:1803-11.

[48] Rosebrock CD, Shirinzadeh S, Soeken M, Riefler N, Wriedt T, Drechsler R, et al. Time-resolved detection of diffusion limited temperature gradients inside single isolated burning droplets using Rainbow Refractometry. Combustion and Flame. 2016;168:255-69.

[49] Li H, Rosebrock CD, Wriedt T, Mädler L. The effect of initial diameter on rainbow positions and temperature distributions of burning single-component n-Alkane droplets. Journal of Quantitative Spectroscopy and Radiative Transfer. 2017;195:164-75.

[50] Wu X, Wu Y, Saengkaew S, Meunier-Guttin-Cluzel S, Gréhan G, Chen L, et al. Concentration and composition measurement of sprays with a global rainbow technique. Measurement Science and Technology. 2012;23:125302.

[51] Ouboukhlik M, Saengkaew S, FournierSalaün MC, Estel L, Gréhan G. Local measurement of mass transfer in a reactive spray for CO2 capture. The Canadian Journal of Chemical Engineering. 2015;93:419-26.

[52] Ouboukhlik M, Godard G, Saengkaew S, Fournier-Salaün M-C, Estel L, Gréhan G. Mass Transfer Evolution in a Reactive Spray during Carbon Dioxide Capture. Chemical Engineering & Technology. 2015;38:1154-64.

[53] Wang J, Gréhan G, Han Y, Saengkaew S, Gouesbet G. Numerical study of global rainbow technique: sensitivity to non-sphericity of droplets. Experiments in Fluids. 2011;51:149-59.

[54] Yu H, Shen J, Tropea C. Application of vector ray tracing to the computation of Möbius shifts for the primary and secondary rainbows. Applied Optics. 2015;54:9093-101.

[55] Lock JA, Können GP. Rainbows by elliptically deformed drops. I. Möbius shift for high-order rainbows. Applied Optics. 2017;56:G88-G97.

[56] Promvongsa J, Vallikul P, Fungtammasan B, Garo A, Gréhan G, Saengkaew S. Multicomponent fuel droplet evaporation using 1D Global Rainbow Technique. Proceedings of the Combustion Institute. 2017;36:2401-8.

[57] Han X, Ren KF, Wu Z, Corbin F, Gouesbet G, Gréhan G. Characterization of initial disturbances in a liquid jet by rainbow sizing. Applied optics. 1998;37:8498-503.

[58] Hulst HC, Van De Hulst H. Light scattering by small particles: Courier Corporation; 1957.

[59] Gouesbet G, Gréhan G. Generalized Lorenz-Mie Theories: Springer; 2011.

[60] Lock JA. Electromagnetic scattering of a plane wave by a radially inhomogeneous sphere in the short wavelength limit. Journal of Quantitative Spectroscopy and Radiative Transfer. 2017;202:126-35.

[61] Li R, Han Xe, Jiang H, Ren KF. Debye series for light scattering by a multilayered sphere. Appl Opt. 2006;45:1260-70.

[62] Xu F, Lock JA, Tropea C. Debye series for light scattering by a spheroid. J Opt Soc Am A. 2010;27:671-86.

[63] Born M, Wolf E. Principles of optics: electromagnetic theory of propagation, interference and diffraction of light: Elsevier; 2013.

[64] Nussenzveig HM. High-Frequency Scattering by a Transparent Sphere. I. Direct Reflection and Transmission. Journal of Mathematical Physics. 1969;10:82.

[65] Nussenzveig H. High-Frequency Scattering by a Transparent Sphere. II. Theory of the Rainbow and the Glory. Journal of Mathematical Physics. 1969;10:125.

[66] Ulmke H, Wriedt T, Bauckhage K. Piezoelectric droplet generator for the calibration of particle-sizing instruments. Chem Eng Technol. 2001;24:265-8.

[67] Riefler N, Wriedt T. Generation of monodisperse micron-sized droplets using free adjustable signals. Part Part Syst Char. 2008;25:176-82.

[68] Tang M, Shiraiwa M, Pöschl U, Cox R, Kalberer M. Compilation and evaluation of gas phase diffusion coefficients of reactive trace gases in the atmosphere: Volume 2. Diffusivities of organic compounds, pressure-normalised mean free paths, and average Knudsen numbers for gas uptake calculations. Atmospheric Chemistry and Physics. 2015;15:5585-98.

[69] Briard P, Saengkaew S, Wu X, Meunier-Guttin-Cluzel S, Chen L, Cen K, et al. Droplet characteristic measurement in Fourier interferometry imaging and behavior at the rainbow angle. Appl Opt. 2013;52:A346-A55.

[70] Kerl K, Varchmin H. Refractive index dispersion (RID) of some liquids in the UV/VIS between 20C and 60C. J Mol Struct. 1995;349:257-60.

[71] Kulmala M, Vesala T, Schwarz J, Smolik J. Mass transfer from a drop-II. Theoretical analysis of temperature dependent mass flux correlation. International Journal of Heat and Mass Transfer. 1995;38:1705-8.

[72] Abarham M, Wichman IS. Mono-component fuel droplet evaporation in the presence of background fuel vapor. International Journal of Heat and Mass Transfer. 2011;54:4090-8.

[73] Pati S, Chakraborty S, Som SK. Influence of ambient vapor concentration on droplet evaporation in a perspective of comparison between diffusion controlled model and kinetic model. International Journal of Heat and Mass Transfer. 2011;54:4580-4.

[74] Roth N, Anders K, Frohn A. Mutual interaction between burning aerosol droplets in the micrometer range. Journal of Aerosol Science. 1989;20:991-4.